Direct determination of dissolution rates at crystal surface using 3D X-ray micro-tomography

Catherine Noiriel [1], Matthias Oursin [1], Giuseppe Saldi [1†] and David Haberthür [2‡]*

[1] Géosciences Environnement Toulouse, Observatoire Midi-Pyrénées, Université Paul Sabatier, CNRS, IRD, 14 avenue Edouard Belin, F-31400 Toulouse, France

[2] Swiss Light Source, TOMCAT beamline, CH-5232 Villigen, Swizerland

KEYWORDS

Calcite dissolution, X-ray micro-tomography, 3D geometry, dissolution rate distribution, surface topography, rate variability

ABSTRACT

Investigations of mineral surface reactivity have recently challenged the classical approach of determining dissolution rates from mineral powders as crystals often exhibit heterogeneous and/or anisotropic reactivity. However, face-specific measurements are restricted to small areas at the surface, limited depth, and ignore the contribution of the crystal edges to the whole process. Here, we provide a detailed characterization of the dissolution kinetics at pH 4.0 of a single calcite crystal in 3D using X-ray micro-tomography with a resolution below 1 µm. The

imaging method allows 3D mapping of the crystal surface topography, providing a description of the time-dependent local dissolution fluxes all over the crystal surface, and the calculation of the crystal dissolution rates. The global rate determined at the crystal scale integrates the contribution of all the crystal features, including the faces, edges and corners, which can be detailed in the local rate distributions. Under acidic conditions, pits develop at the $\{10\bar{1}4\}$ surface, before dissolution tends to smooth out both the crystal surface asperities and the edges and corners. In addition, a high rate variability is noticed over the crystal surface. The heterogeneous dissolution rates at the crystal surface first led to a local increase of the surface roughness due to pit formation and coalescence, followed by a decrease of the global crystal roughness due to smoothing of the large-scale surface asperities, crystal edges and corners. Etch pits dominate initially the surface topography, whereas the evolution of the crystal morphology is dominated by the reactivity of edges and corners, whose contribution to dissolution is on average 1.7 to 3.6 times higher than the crystal faces. These results suggest that dissolution reaction preferentially occurs at the crystal edges and corners, something not considered in most studies of mineral dissolution.

1. INTRODUCTION

Mineral reactivity is an important parameter to account for in modeling of major natural or anthropogenic geological processes such as continental weathering, diagenesis, aquifer contamination, geothermal energy production, carbon dioxide sequestration or nuclear waste disposal [1-3]. In this perspective, evaluation of reaction kinetics has received much attention over the past four decades, in particular to provide reactive transport codes with reliable parameters to evaluate chemical reactivity over large space and time scales. However, discrepancies between

rates determined in well-controlled conditions, up to several orders of magnitude, have long been reported. A number of causes have been proposed to explain these inconsistencies, such as differences in experimental setup or sample preparation, mass-transport limitations, surface passivation, differences in surface normalization methods, changes in reactive surface area, presence of inhibitors or catalysts [4-6], or crystallographic and micro-structural control of mineral reactivity [7, 8].

Advances in microscopic techniques such as atomic force microscopy (AFM) [9-11], vertical scanning interferometry (VSI) [12, 13], confocal profilometry [14] X-ray reflectivity [15], digital holographic microscopy [16] or X-ray microscopy [17] have enabled measurements of rates on face-oriented crystals. Investigations of crystal reactivity using these techniques, together with increasing computation methods like kinetic Monte Carlo (KMC) modelling [18-20], have recently challenged the classical approach of determining reaction rates from bulk experiments on mineral powders, as crystals often exhibit heterogeneous and/or anisotropic reactivities which reflects the diversity of energetic sites and reaction mechanisms [21, 22].

Study of the cleaved $\{10\bar{1}4\}$ surface of calcite, for instance, has permitted investigation of the role of solution chemistry in the formation of etch pits and the kinematics of step retreat during dissolution under a large variety of experimental conditions [5, 9, 11, 13, 23-32]. However, face-specific measurements are often restricted to small surface areas (typically less than 500 × 500 μm^2) at the single crystal face, may have limited vertical range (e.g., about 5 µm for AFM), and ignore the contribution of the crystal edges and corners to the whole process [8], so that the possible variation in reaction mechanisms is restricted to nm- to µm-scale observations, and upscaling of the observations and rates determined from 2D techniques on single faces to mineral, porous rock, or reservoir scale remains challenging.

Non-invasive and non-destructive 3D X-ray micro-tomography (XMT) imaging has demonstrated its usefulness to direct visualization of fluid–mineral interface in rocks or rock aggregates [33-40], and the technique can be extended to single crystal observations. Although a compromise has to be made between the imaging resolution (pixel size) and the acquisition time, the development of fast detection systems, high quality optics, and high data rate streaming has recently increased the capabilities for sub-second imaging or nano-imaging experiments [41, 42]. The great potential of the method should allow the *in situ* dynamic tracking of fast reactions with a micrometric resolution, as well as the study of slower reactions with sub-micrometric resolution (i.e., with a pixel size up to about 50 nm) at well-spaced intervals. In the latter case, several control points (or landmarks) must be identified within the crystal or at the crystal surface to allow the registration of 3D data sets, as the sample will have to be removed from the beamline between two acquisition times.

We present the first direct 3D measurements of mineral dissolution, using a calcite crystal specimen in dissolution experiments at pH 4.0 and far-from-equilibrium conditions. As opposed to traditional methods to track the evolution of mineral surface topography (e.g., AFM, VSI or holographic microscopy), our study benefits from the use of XMT imaging to monitor the dissolution kinetics of the whole single crystal over time in a true 3D space, following the application of the technique to track the mineral/water interface [33]. With the given imaging resolution and crystal size, almost 5 million discretized data points were analyzed at the crystal surface. The technique has an unlimited depth of investigation at the crystal surface, which makes it possible to follow-up pit formation and evolution at the surface as well as the evolution of macro-features and of crystal edges and corners over time. In addition, no specific preparation of the sample that could alter its surface reactivity (e.g., polishing) is required. With registration

of the 3D volumes into the same coordinate system, the technique permits a direct monitoring of the localized changes over the whole mineral surface and to calculate the local rates of dissolution at the mineral surface.

2. METHODS AND MATERIAL

2.1 SAMPLE PREPARATION AND DISSOLUTION EXPERIMENT

A cleaved single calcite crystal about half a millimeter long was obtained after crushing and sieving a cm-sized single spar crystal. The crystal was ultrasonically cleaned and washed with deionized water prior to the experiment. It was mounted on a glass capillary tube (Hilgenberg, 400 µm O.D.) using epoxy glue, which partially covered one corner region of the crystal creating a mask that preserved a portion of the surface from dissolution. Note that the crystal faces were not polished before the experiment, so that they exhibit various macro-features such as cleavage ragged macro-steps, hillocks, curved "super-steps" and rippled surface patterns, which were inherited from the breaking and size reduction of the original calcite sample (see below Figure 2a).

The crystal was reacted at five time steps (t_1 to t_5) of 1, 3, 6, 9 and 12 hours with an acidic solution (pH = 4.0) in a mixed-flow reactor (V = 160 mL) at room temperature (25 ± 3°C) and atmospheric pressure. The flow rate was set to Q = 8 $cm^3 \cdot h^{-1}$ and the stirring rate to 400 rpm during the experiment to impose far-from-equilibrium conditions. The inlet solution was prepared with deionized water (18.2 MΩ·cm) + 0.01M NaCl, and the pH was adjusted to 4.0 ± 0.1 using analytical grade HCl. Note that, because of the high fluid volume to mineral surface ratio, the Ca concentration in samples collected during the experiment and analyzed by ICP-MS (inductive coupled plasma-mass spectroscopy) varied only between 1.0×10^{-5} and 2.9×10^{-5} M

over the course of the reaction, keeping the fluid at far-from-equilibrium conditions. The corresponding saturation ratio (Ω) with respect to calcite, as calculated by Phreeqc v3.0 using the Phreeqc database [43], remained indeed below 10^{-9} throughout the experiment, thus excluding any appreciable effect of the fluid chemical evolution on the dissolution rates.

2.3 X-RAY MICRO-TOMOGRAPHY IMAGING

The crystal was imaged before the reaction (t_0) and at the five time steps of the dissolution experiment using 3D X-ray micro-tomography at the TOMCAT beamline [44], Swiss Light Source (Paul Scherer Institute, Switzerland). A total of 6 data sets were collected (t_0 to t_5). Each data set is composed of 1701 radiographs collected over a 180° rotation range. Each radiograph was recorded with a monochromatic and parallel beam at the energy of 20 keV and an exposure time of 200 ms. After penetration of the samples, the X-rays were converted into visible light with a LuAG:Ce scintillator. The visible light was magnified using ×10 magnification diffraction-limited microscope optics and recorded with a sCMOS camera of 2560×2160 pixels. The resulting pixel size (optical resolution) was thus 0.65 µm. Volume reconstruction was performed from the radiographs corrected from flat field and background noise using an algorithm based on the Fourier transform method [45].

After reconstruction, image processing was carried out with Avizo® software on data sets of 1650×600×1900 voxels. First, the 3D grayscale volumes were normalized, converted to 8-bit integers, and denoised with a 3D median filter using a kernel size of 3×3×3 pixels. Then, the crystals were registered in the same coordinate system, using the capillary glass and chemically inert masked area as a fixed reference. Data were segmented using a threshold value halfway between the two maximum peaks for air and calcite to provide a discretized geometry of the

crystal. After segmentation, the solid objects, i.e., crystal and capillary glass, were labeled in order to separate and remove the capillary glass from the image.

The crystal volume $V_{crystal}$ (μm^3) is calculated from the number of element solid voxels n_{sol}: $V_{crystal} = n_{sol} \times V_{voxel}$, with V_{voxel} the volume of a voxel (0.65×0.65×0.65 μm^3). The crystal surface area (μm^2) is calculated from the number of solid-air pixel interfaces: $S_{crystal} = n_{sol-air} \times S_{pixel}$, with S_{pixel} the surface area of a pixel (0.65×0.65 μm^2), which is the smallest element of surface area at the fluid-crystal interface. Note that the volume and surface area of the unreacted part of the crystal (mask) were not considered in the calculations.

2.4 DISSOLUTION RATES FROM 3D IMAGING

The global crystal dissolution rate r_{diss} (mol·s^{-1}) and rate normalized to the surface area of the crystal $r_{diss-norm}$ (mol·m^{-2}·s^{-1}) were calculated after segmentation of the data sets according to the following equations:

$$r_{diss} = \frac{\Delta V_{crystal}}{\upsilon_{cal}\,\Delta t} \qquad (1)$$

and

$$r_{diss-norm} = \frac{\Delta V_{crystal}}{\overline{S_{crystal}}\,\upsilon_{cal}\,\Delta t}, \qquad (2)$$

where υ_{cal} is the molar volume of calcite (m^3·mol^{-1}) and $\overline{S_{crystal}}$ is the average crystal surface area (m^2) between two stages of dissolution.

In addition, the local dissolution rate r'_{diss} ($\mu m \cdot h^{-1}$ or $nm \cdot s^{-1}$) was determined at any element (i.e., fluid-crystal pixel interface) of the crystal surface, according to the following procedure. First, the 3D Euclidean distance map inside the crystal was computed from the fluid-crystal interface at t_0 based on a 3-4-5 Chamfer distance transform [46, 47]. Consequently, each voxel inside the unreacted crystal is labeled with the distance to its nearest boundary pixel, starting from the position of the fluid-unreacted crystal interface. The distance transform corresponds to a quasi-uniform scaling of the crystal. Combining the distance map with the position of the fluid-crystal interface at any stage of experiment, t_i, gives the surface retreat of the crystal normal to the crystallographic surfaces of the unreacted crystal, as illustrated in Figure 1. Then, the local dissolution rate was calculated according to:

$$r'_{diss} = \frac{d\,\mathbf{I_{fc}} \cdot \mathbf{n}}{dt}, \qquad (3)$$

with $\mathbf{I_{fc}}$ the fluid-crystal position vector, and $\mathbf{n}$ the normal to the crystal $\{10\bar{1}4\}$ surface.

The local dissolution rates were computed at each experiment stage using the unreacted crystal at t_0 as a reference. Since the number of fluid-crystal interface pixels decreases as dissolution progresses and the bin width of the histograms decreases with increasing dt, the dissolution rate distributions were normalized to the distribution at t_2 to allow for a better visualization.

Extraction of a surface portion of 260 × 325 μm^2 was also done for the visualization of the local topography evolution. In that case, the mean surface plane at t_0 was referenced to a horizontal surface for the calculation of the etch pits depth. The transformation was applied to any other surface extracts at t_i.

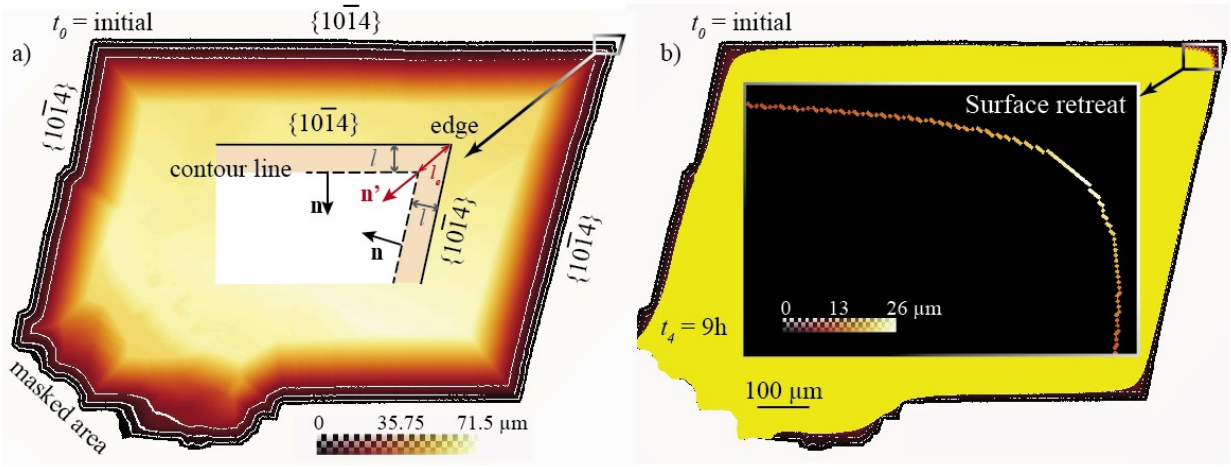

Figure 1. Schematic view (2D cross-section) of the distance transform procedure to calculate the surface retreat between two stages of dissolution. (a) 3D distance map of the unreacted crystal, which represents the shortest distance of each voxel inside the crystal to the fluid-solid interface at t_0. Distance contours of 10, 25, and 50 pixels (white lines) are shown to highlight that due the quasi-uniform scaling of the crystal, the distance measured at the edges (see the schematic representation in the insert) is actually the normal-distance to the neighboring surface $\{10\bar{1}4\}$, i.e., l, not the normal-distance to the edge itself, i.e., l_e. (b) Combining the distance map with the crystal at t_4 (yellow) gives the retreat at the crystal surface (see details in the insert). **n** is the normal to the $\{10\bar{1}4\}$ crystal surface, **n'** is the normal to the edge.

3 RESULTS AND DISCUSSION

3.1 EVOLUTION OF SURFACE TOPOGRAPHY AND CRYSTAL MORPHOLOGY

The average surface retreat reaches 17.2 µm at t_5, while dissolution proceeds with heterogeneous surface retreat at different scales (Figure 2).

At the face-scale, the surface topography exhibits the features commonly reported in the literature [9, 32] (Figure 2b). At t_1, a high density of small etch pits of about 2-15 µm in size (about 2400 per mm^2 as calculated in the surface extract) develops by preferential dissolution at specific locations heterogeneously distributed at the surface. The high density of pits might be linked to defects (i.e., dislocation, point defects or impurity clusters) existing at the surface or created during preparation of the specimen, although spontaneous pit formation is also possible at non-dislocation sites [28]. Indeed, the low saturation index of the fluid in the experiment ($\Omega < 10^{-9}$) is compatible with the unassisted pit formation reported by Teng et al. [28] at saturation index $\Omega <$ 0.007, the critical saturation index of which the energy released from dissolution-induced chemical bond disassociation may be sufficient enough to offset the energy barrier for etch pits at non-dislocation sites.

From t_1 to t_2, some rhombohedral pits grow laterally and in depth with time, whereas others disappear. At t_2, the density of pits has decreased to 630 per mm^2. From t_1 to t_4, some pits keep growing faster in depth than the global surface retreat (e.g., Figure 2, insert 2 at t_2), so that their depth increases slightly, up to about 4 µm, while the global surface retreat is ~15 µm; in contrast, some other pits are not visible anymore (e.g. Figure 2, insert 2 at t_3). The heterogeneity in the pit growth rate compared to the average surface retreat points to likely nucleation mechanisms at the pit tip, as observed, for instance, by MacInnis and Brantley [48]. It is also worth noting that defects underlying the extant crystal surface may at some point contribute to the heterogeneity of

dissolution (for instance, see the arrays of pits along cleavage defects which appeared at the surface from t_2 in Figure 2).

With further reaction these pits progressively merge into less numerous macro-pits of about 20-40 μm in size and finally annihilate (Figure 2b). The anisotropy in step velocities between obtuse and acute steps developed parallel to the crystallographic directions $[\bar{4}41]$ and $[48\bar{1}]$, which results in asymmetrical pit formation is also noticed (Figure 2b), in agreement with previous AFM and VSI observations [11, 26]. New pits continuously form and develop over the surface (for instance, see the array of pits highlighted at t_5 in Figure 2a), although the high density of pits observed at t_1 is no longer attained at this stage of the reaction. At t_5, the density of macro-pits has decreased to 130 per mm^2.

At the crystal scale, dissolution of macro-features such as curved macro-steps is faster than the average vertical retreat of the surfaces, so that the crystal macro-asperities as well as the crystal edges and corners tend to become smoother with time (Figures 2a-2b). As a result, the crystal becomes rounder. In contrast, dissolution in topographic lows or at the base of macro-steps is slower. The pits become also less visible, except for a few macro-pits and linear arrays of pits along cleavage defects (t_4-t_5). In fact, the development of numerous steps over the surface progressively gives to the crystal surface a smooth and rounded shape (e.g., as visible in the bottom and right parts of Figure 2b at t_4) that annihilates the development of macro-pits which vanish either by coalescence or by intersection with a train of steps coming from near-edge regions [32].

Both surface pitting and crystal smoothing result in an increase of the surface roughness. Indeed, the surface roughness of the 260 × 325 μm^2 extract, defined as the standard deviation of the

224 distributions of the surface heights, increases continuously throughout the experiment, from 0.50
225 to 0.81 µm between t_0 and t_2 due to surface pitting, and from 1.04 to 2.22 µm between t_3 and
226 t_5 due to a large-scale increase in the crystal surface curvature (as visible in Figure 2b at t_4) and
227 a gross shift to a more rounded geometry of the crystal. The apparent surface roughness increase
228 between t_3 and t_5 while the crystal surface becomes smoother appears somewhat contradictory,
229 but result actually of the inadequate definition of surface roughness, which was normalized to the
230 mean surface plane and not to the mean crystal curvature in the present study. Overall, the
231 progressive smoothing of the $\{10\bar{1}4\}$ surfaces is consistent with the simulation of de Assis and
232 Aarao Reis [49] for rough surfaces, where the decrease of the kink site fraction with high energy
233 and the increase of the step-edge site and terrace fractions with low energy make the rough
234 surface evolve to a flat configuration.

235

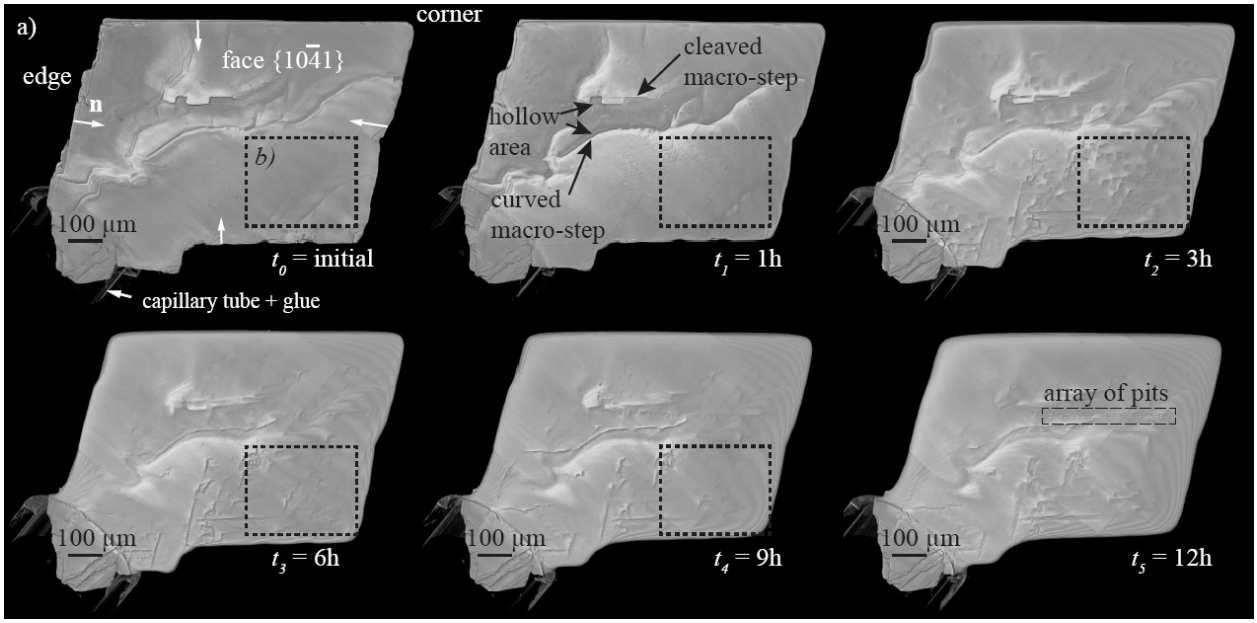

236

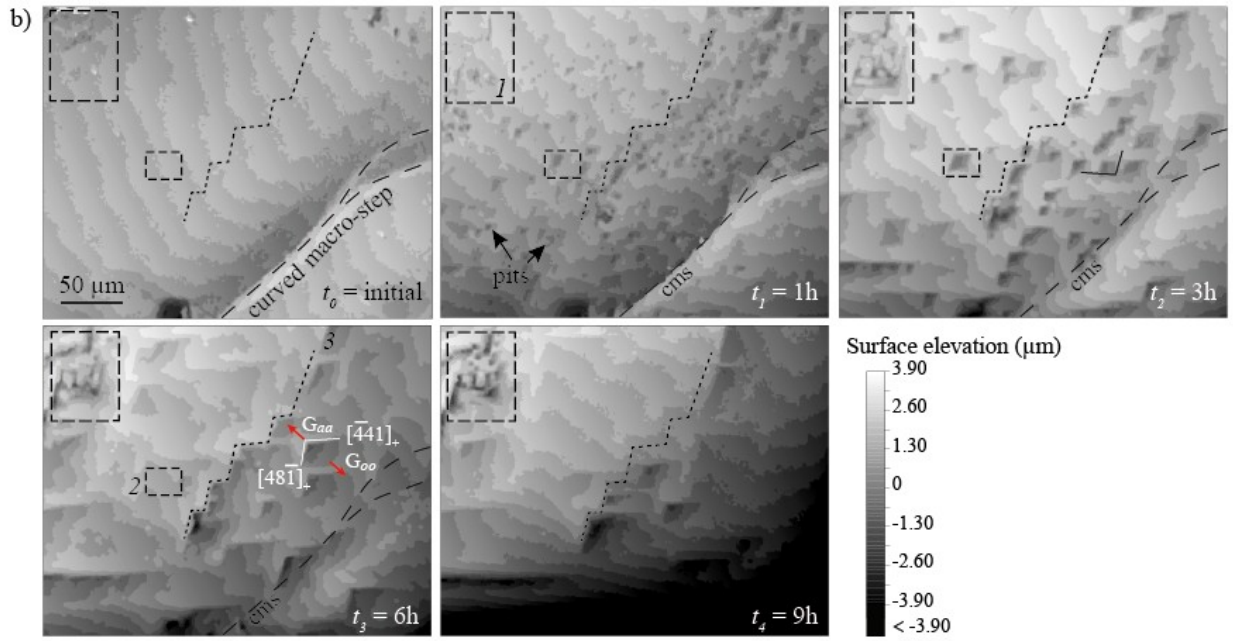

Figure 2. (a) 3D rendering view of the calcite crystal specimen at the different times of experiment (t_0 to t_5); the surface topography shown in (b) is highlighted in the dashed square. (b) Detailed surface topography evolution between t_0 and t_4 showing etch pit formation, merging and annihilation with time. Insert *1* shows the development of a high-density pitted area below the unreacted surface. Insert *2* shows pit formation and growth between t_1 and t_2, and annihilation between t_2 and t_3. Insert *3* (dotted line) highlights the position of pits at t_3 and is reported in the other images for comparison.

3.2 DISSOLUTION RATE AND RATE DISTRIBUTION

Dissolution results in a decrease of both the crystal volume and surface area, but the global dissolution rate, r_{diss}, does not change substantially, with an average dissolution rate $\bar{r}_{diss}$ of 2.19 10^{-11} ± 0.27 10^{-11} mol·s^{-1} over the experiment duration (Table 1). The average surface area

normalized rate, $\bar{r}_{diss-norm}$, is equal to 1.26 10^{-5} ± 0.20 10^{-5} mol·m^{-2}·s^{-1}. The value is lower than the data of Plummer et al. [50] (5.23 10^{-5} mol·m^{-2}·s^{-1}) or Chou et al. [51] (8.97 10^{-5} mol·m^{-2}·s^{-1}) determined on powders, but higher than the AFM-derived data of De Giudici [52] (3.16 10^{-6} mol·m^{-2}·s^{-1}). These differences are certainly due to both (i) differences in experimental conditions, and (ii) the procedure of normalization of the specific surface, as already discussed by Arvidson et al. [5] or Colombani [53]. The specific surface area of the unreacted crystal determined at the scale of the XMT imaging technique is 46.8 cm^2·g^{-1}, which is lower than the surface area of 120 cm^2·g^{-1} determined by BET method [54] on similar calcite crystals [37]. Using the BET surface area as a reference for normalization would reduce in this case the rate by a factor of 2.56. However, the normalized rate is in agreement with the rate obtained by Shiraki et al. [11] (1 10^{-5} mol·m^{-2}·s^{-1}) from the calcium released during dissolution of cleaved crystals of 2-3mm in dimension. In their experiments, Shiraki et al. [11] observed that the rates obtained from calcium flux were about a factor of three higher than the rates based on micro-topography determined by AFM at all pH values, albeit the sides of the crystals were coated with epoxy; however, it is worth mentioning that they used a simple geometric surface to normalize the rates calculated form Ca fluxes. As suggested by Dove and Platt [30], the apparent lower reactivity obtained stems from the fact that AFM observations are restricted to smooth and planar areas at the mineral surface, which have less reactive sites.

More interesting is the determination of local dissolution rates at the crystal surface, which provides an instantaneous capture of the dissolution process. The average local dissolution rate of the crystal, $\bar{r}'_{diss}$, varies between 1.24 and 1.46 µm h^{-1} (0.34 and 0.40 nm s^{-1}) during the experiment (Table 1). However, the distribution of local dissolution rates is highly heterogeneous over the crystal surface. The different surface retreats result from the heterogeneous distribution

of the reaction over the surface between two stages of dissolution (Figure 3a). Figure 3b presents the local rate distribution mapped on the crystal at t_4. We can notice heterogeneities both at the face scale and at the crystal scale, as already suggested by the topography evolution.

The local rate distributions for each reaction time step are shown in Figure 3c. At t_1, the distribution is not well defined due to very small retreat at the crystal surface. In a similar way, the distribution is not well defined near zero for t_2. From t_2, the histograms are bell-shaped with a long tail. No substantial changes in the dissolution rate distributions are noticed with time. The rates are comprised between 0 (masked area) and 5 µm h^{-1}, with the peak maximum at about 1 µm h^{-1}. Contrary to the rate distribution obtained from VSI or AFM measurements on single faces or polished limestone surfaces [21, 55, 56], named as rate spectra, the distributions presented here highlight the contribution of all the different crystal features to the dissolution process. In particular, the contribution of the faces, edges and corners can be quantified and compared to each other. For instance, between t_0 and t_4, the average local dissolution rate is 1.45 µm.h^{-1} (Figure 3d). At the same time, the contribution of the face, edge and corner identified in three volumes of interest (VOIs) is on average 0.87, 1.52, and 3.14 µm.h^{-1}, respectively (Figure 3d). This means also that the maximum rate of 5 µm h^{-1} measured at one corner is 5.74 times faster than the average face retreat (Figure 3c). The local rates differ by less than one order of magnitude, similarly to what has been observed for calcite single crystals in VSI experiments [6, 55, 56], with the exception of slow dissolving material [56] where the dissolution rate distribution spread over several orders of magnitude near zero due to vertical resolution limitations (as it is the case in our experiment at t_1 and t_2).

In addition, there is a factor of ten at maximum between the highest surface retreat at corner and the slowest $\{10\bar{1}4\}$ surface retreat. This value is, however, too low to explain the order of magnitude difference between the rates derived from batch experiments on powders [50, 51] and those determined from AFM on single faces [11, 52].

Dissolution at the crystal edges and corners is known to increase the population of step and kink sites over time, as already suggested by Arvidson et al. [5] or observed after KMC dissolution modeling of cubic crystals [20, 57], a hypothesis consistent with larger dissolution rates at the edges and corners. In addition, dissolution of calcite at pH 4.0 is diffusion-limited [50, 58], so that the edges and corners might experience a higher diffusive flux at their surface, in relation with the near-surface hydrodynamic conditions of the experiment. This could also explain why the topographic lows at the crystal surface dissolve more slowly than their adjacent flat terraces, although they might also coincide with lower energy site areas [49, 59]. In fact, both cases might explain the observed lower reactivity. In addition, it is worth noting that the higher dissolution rates at the edges do not affect only the vicinity of the edges themselves. Indeed, Figure 3b clearly shows that the surface retreat is less and less pronounced from the edges toward the face centre. The high density of steps at the edges constitutes a large source of dissolution stepwaves [60] that propagate from the edges throughout the mineral surface. As a result, the crystal surface becomes progressively dominated by steps and kinks, whose dynamics controls the dissolution process. It is worth noting that distinguishing the edges and corners from the $\{10\bar{1}4\}$ surfaces becomes somehow difficult at some point, as the transition between these features fades with the progressive crystal rounding. Overall it is expected that a higher population of kinks and steps develops from the edges and corners toward the center of the $\{10\bar{1}4\}$ faces as long as dissolution progresses (and the crystal size decreases), similarly to what can be shown at nano-scale [61]. This

317 would imply an increase in the dissolution rate, although this does not seem high enough to be
318 recorded in the present experiment.

319 4. CONCLUSION

320 We have presented the first time-resolved 3D characterization of mineral dissolution, using a
321 calcite crystal dissolving at pH 4.0 as a specimen. During the 12-hour dissolution experiment,
322 heterogeneous dissolution rates at the crystal surface first led to a local increase of the surface
323 roughness due to pit formation and coalescence, followed by a decrease of the global crystal
324 roughness due to smoothing of the large-scale surface asperities, crystal edges and corners. The
325 global rate determined at the crystal-scale integrates the contribution of all the crystal features,
326 including the $\{10\bar{1}4\}$ faces, edges and corners, which can be detailed in the local rate
327 distributions.

328 Our results show that etch pits dominate initially the surface topography, whereas the evolution
329 of the crystal morphology is dominated by the reactivity of edges and corners. Their contribution
330 to dissolution is on average 1.7 to 3.6 times higher than the faces due to the more numerous steps
331 and kinks which form at their surface. Under the studied conditions, the edges are the main
332 sources of steps moving over the surface, and the stepwave propagation drives the dissolution
333 process, with the faces becoming progressively dominated by steps instead of etch pits. The
334 decrease of the large amount of pits present at t_1 is thus the result of the obliteration by the steps
335 moving from the edges towards the center of the crystal face. The diffusive flux may also be
336 enhanced under transport-limited conditions at the edges and corners, thus enhancing smoothing
337 of these initial sharp features.

This experiment shows that at pH 4.0 the contribution of edges and corners to dissolution is more important than the contribution of single faces. There is a factor of ten at maximum between the highest surface retreat at corner and the slowest $\{10\bar{1}4\}$ surface retreat. This value is, however, too low to explain the order of magnitude difference between the rates derived from batch experiments on powders [50, 51] and those determined from AFM on single faces [11, 52]. Surface normalization must be sought as a bigger source of discrepancy compared to experimental methods.

This present study contributes to an emerging body of work demonstrating how mineral reactivity is a complex, non-isotropic process that cannot be reduced to localized observations at the crystal surface. It demonstrates that application of time-resolved X-ray micro-tomography imaging is providing detailed insights on the dissolution mechanisms at the mineral scale (i.e., including the whole geometry of the crystal) and should improve the determination of kinetic rates. In particular we expect that the observed rate distributions across the edges and corners will be helpful to constrain kinetic KMC simulations based on bond-breaking [62] or to define rates more representative of the dynamics of crystal evolution.

These results may enhance our understanding of mineral reactivity, which is of primary importance when considering long term storage security of carbon dioxide in the subsurface. Numerical models for CO_2-induced dissolution requires reliable reaction rates for minerals, and data derived from 3D XMT imaging can provide fundamental information to develop more accurate prediction models. By identifying and integrating the contribution of crystal face, edges and corners to the whole dissolution process, 3D XMT imaging adds a new dimension in the dynamic study of mineral reactivity, with the expectation to obtain more reliable data and facilitate the reconciliation between rates derived from observations at the mineral surface and

those derived from bulk experiment on powders. This work should have implications for the reactive transport modeling of dissolution in rocks, especially in well-crystallized limestone, in which crystal edges, grain boundaries and corners of fibrous, bladed or equant spar cements are directly in contact with the advective fluids. In this petrophysical context, for instance, the edges and corners of the first crystal layer within a pore (corresponding the surface directly exposed to the flowing fluid) could be more exposed to the advective fluid, whereas their adjacent $\{10\bar{1}4\}$ faces, as the underling crystals (corresponding the grain boundaries) will be dominated by diffusive transport.

The results also demonstrate that X-ray micro-tomography is a useful tool to track the fluid-mineral interface evolution during geochemical processes at the crystal scale and will be helpful to link the observations and measurements obtained at the nm- and µm-scale on mineral single faces to the reactivity of the whole mineral, mineral powders, and mono-mineral rocks. In this regard, it might constitute a nice bridge between micro-scale surface topography observations (e.g., with AFM or VSI) and powder studies in continuously stirred reactor, and could be helpful to gain a broad, unified, mechanistically, and statistically relevant picture of dissolution kinetics over multiple length scales. This methodology could be extended to the dissolution/precipitation study of other minerals, crystals or rock aggregates, especially those which display heterogeneous and/or anisotropic reactivity.

Table 1. Summary of the experimental results

Stage	Time (h)	Volume (m^3)	Area (m^2)	r_{diss} ($mol.s^{-1}$)	$r_{diss-norm}$ ($mol.m^{-2}.s^{-1}$)	$\bar{r}'_{diss}$ ($\mu m.h^{-1}$)

initial t_0	0	$1.55\ 10^{-10}$	$1.97\ 10^{-6}$			
t_1	1	$1.53\ 10^{-10}$	$1.92\ 10^{-6}$	$1.91\ 10^{-11}$	$9.85\ 10^{-6}$	1.46
t_2	3	$1.47\ 10^{-10}$	$1.81\ 10^{-6}$	$2.12\ 10^{-11}$	$1.14\ 10^{-5}$	1.24
t_3	6	$1.37\ 10^{-10}$	$1.70\ 10^{-6}$	$2.60\ 10^{-11}$	$1.48\ 10^{-5}$	1.40
t_4	9.03	$1.27\ 10^{-10}$	$1.61\ 10^{-6}$	$2.33\ 10^{-11}$	$1.41\ 10^{-5}$	1.45
t_5	12.03	$1.19\ 10^{-10}$	$1.53\ 10^{-6}$	$2.00\ 10^{-11}$	$1.28\ 10^{-5}$	1.43

381

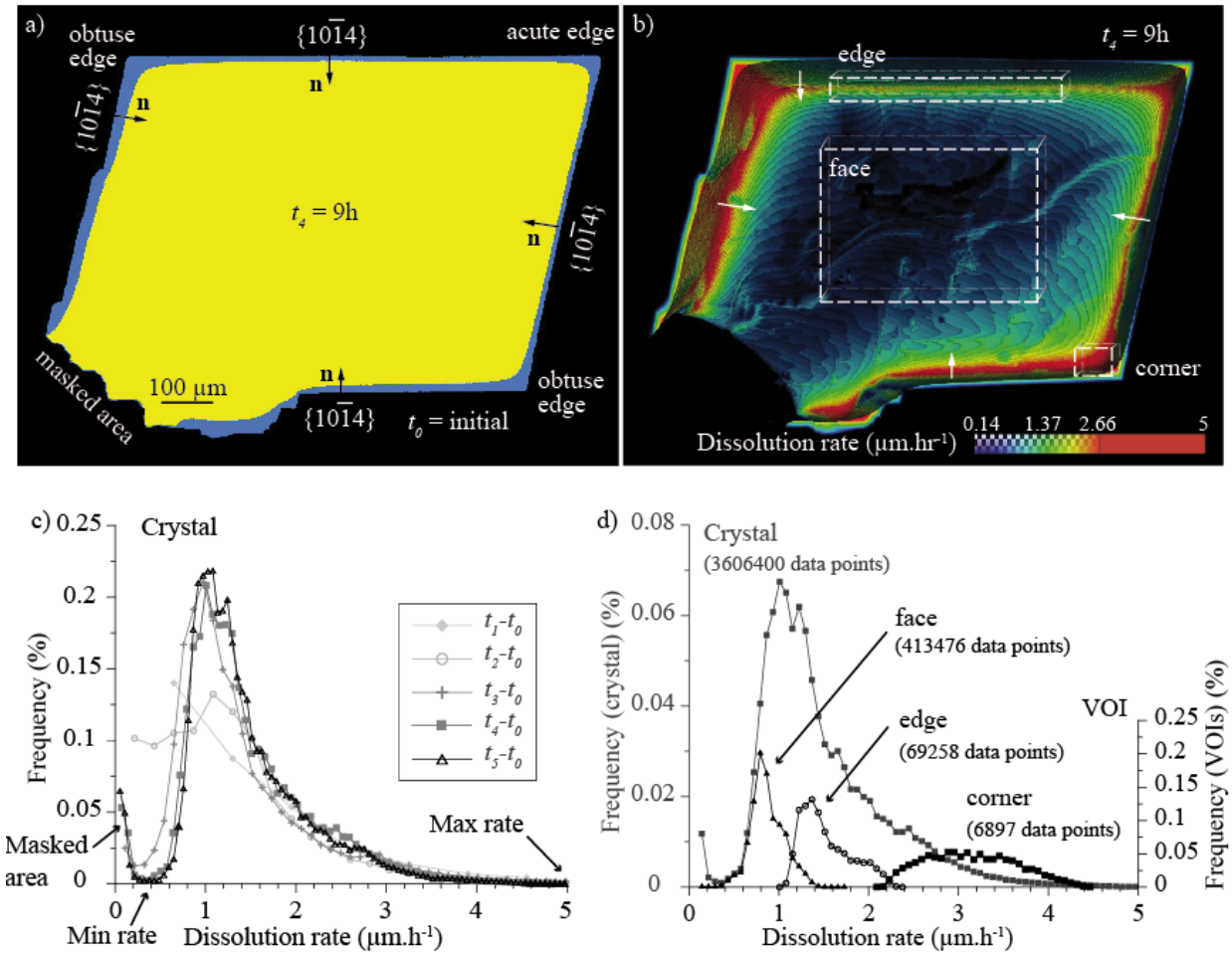

382

383 **Figure 3**. (a) Cross-section of the crystal at t_0 (blue) and t_4 (yellow, superimposed), showing the
384 crystal surface retreat heterogeneity normal to the surfaces $\{10\bar{1}4\}$. (b) Local dissolution rate
385 mapped over the crystal surface at t_4; the front face of the crystal has been cut out and the image
386 has been vertically flipped to allow comparison with Figure 2; three selected volumes of interest
387 (VOIs) whose rate data are presented in (d) are localized in the image. (c) Dissolution rate
388 distributions at the different times of the experiment normalized to the distribution at t_2. (d)
389 Detailed contribution of the face, edge and corner identified in the VOIs at t_4; the histograms are
390 normalized for the sake of visualization, and the number of data points used in the calculation of
391 the histograms is also indicated.

392

393 AUTHOR INFORMATION

394 **Corresponding Author**

395 * Catherine Noiriel (catherine.noiriel@univ-tlse3.fr)

396 **Present Addresses**

397 † Now at University College London, Department of Earth Sciences, London

398 ‡ Now at Institute of Anatomy, University of Bern, Switzerland

399

400 ACKNOWLEDGMENT

401 This work was funded by the Institut Carnot ISIFOR under contract SEQFRAC 400034. We
402 acknowledge the Paul Scherrer Institute for provision of synchrotron radiation beamtime at
403 Swiss Light Source, TOMCAT beamline X02DA. We also kindly acknowledge the comments
404 and suggestions made by the four reviewers, which were helpful in improving the manuscript.

405

406 ABBREVIATIONS

407 AFM atomic force microscopy; ICP-MS inductive coupled plasma-mass spectroscopy; KMC
408 kinetic Monte Carlo; VOI volume of interest; VSI vertical scanning interferometry; XMT X-ray
409 micro-tomography.

410

411 REFERENCES

412 1. DePaolo, D. J.; Orr, F. M., Geoscience research for our energy future. *Physics Today*
413 **2008,** *61* (8), 46-51.

414 2. Steefel, C. I.; DePaolo, D. J.; Lichtner, P. C., Reactive transport modeling: An essential
415 tool and a new research approach for the Earth sciences. *Earth Planet. Sci. Lett.* **2005,** *240* (3-4),
416 539-558.

417 3. Noiriel, C.; Daval, D., Pore-scale geochemical reactivity associated with CO_2 storage:
418 New frontiers at the fluid-solid interface. *Accounts of Chemical Research* **2017,** *50* (4), 759-768.

419 4. White, A. F.; Brantley, S. L., The effect of time on the weathering of silicate minerals:
420 Why do weathering rates differ in the laboratory and field? *Chem. Geol.* **2003,** *202*, 479-506.

421 5. Arvidson, R. S.; Evren Ertan, I.; Amonette, J. E.; Lüttge, A., Variation in calcite
422 dissolution rates: A fundamental problem? *Geochim. Cosmochim. Acta* **2003,** *67* (9), 1623-1634.

423 6. Fischer, C.; Arvidson, R. S.; Lüttge, A., How predictable are dissolution rates of
424 crystalline material? *Geochim. Cosmochim. Acta* **2012,** *98*, 177-185.

425 7. Pollet-Villard, M.; Daval, D.; Ackerer, P.; Saldi, G. D.; Wild, B.; Knauss, K. G.; Fritz,
426 B., Does crystallographic anisotropy prevent the conventional treatment of aqueous mineral
427 reactivity? A case study based on K-feldspar dissolution kinetics. *Geochim. Cosmochim. Acta*
428 **2016,** *190*, 294-308.

429 8. Saldi, G. D.; Voltolini, M.; Knauss, K. G., Effects of surface orientation, fluid chemistry
430 and mechanical polishing on the variability of dolomite dissolution rates. *Geochim. Cosmochim.*
431 *Acta* **2017,** *206*, 94-111.

432 9. Hillner, P. E.; Gratz, A. J.; Manne, S.; Hasma, P. K., Atomic-scale imaging of calcite
433 growth and dissolution in real time. *Geology* **1992,** *20*, 359-362.

434 10. Stipp, S. L. S.; Eggleston, C. M.; Nielsen, B. S., Calcite surface observed at
435 microtopographic and molecular scales with atomic force microscopy (AFM). *Geochim.*
436 *Cosmochim. Acta* **1994,** *58* (14), 3023-3033.

11. Shiraki, R.; Rock, P. A.; Casey, W. H., Dissolution kinetics of calcite in 0.1M NaCl solution at room temperature: An atomic force microscopic (AFM) study. *Aquatic Geochemistry* **2000,** *6*, 87-108.

12. Fischer, C.; Luttge, A., Converged surface roughness parameters - A new tool to quantify rock surface morphology and reactivity alteration. *Am. J. Sci.* **2007,** *307* (7), 955-973.

13. Smith, M. E.; Knauss, K. G.; Higgins, S. R., Effects of crystal orientation on the dissolution of calcite by chemical and microscopic analysis. *Chem. Geol.* **2013,** *360*, 10-21.

14. Godinho, J. R. A.; Piazolo, S.; Evins, L. Z., Effect of surface orientation on dissolution rates and topography of CaF2. *Geochim. Cosmochim. Acta* **2012,** *86*, 392-403.

15. Fenter, P.; Geissbühler, P.; DiMasi, E.; Srajer, G.; Sorenssen, L. B.; Sturchio, N. C., Surface speciation of calcite observed in situ by high-resolution X-ray reflectivity. *Geochim. Cosmochim. Acta* **2000,** *64* (7), 1221-1228.

16. Brand, A. S.; Feng, P.; Bullard, J. W., Calcite dissolution rate spectra measured by in situ digital holographic microscopy. *Geochim. Cosmochim. Acta* **2017,** *213*, 317-329.

17. Laanait, N.; Callagon, E. B. R.; Zhang, Z.; Sturchio, N. C.; Lee, S. S.; Fenter, P., X-ray–driven reaction front dynamics at calcite-water interfaces. *Science* **2015,** *349* (6254), 1330-1334.

18. Kurganskaya, I.; Luttge, A., Kinetic Monte Carlo approach to study carbonate dissolution. *The Journal of Physical Chemistry C* **2016,** *120* (12), 6482-6492.

19. Luttge, A.; Arvidson, R. S., Reactions at surfaces: A new approach integrating interferometry and kinetic simulations. *Journal of the American Ceramic Society* **2010,** *93* (11), 3519-3530.

20. Lüttge, A.; Arvidson, R. S.; Fischer, C., A stochastic treatment of crystal dissolution kinetics. *Elements* **2013,** *9* (3), 183-188.

21. Fischer, C.; Kurganskaya, I.; Schaefer, T.; Lüttge, A., Variability of crystal surface reactivity: What do we know? *Appl. Geochem.* **2014,** *43*, 132-157.

22. Pollet-Villard, M.; Daval, D.; Fritz, B.; Knauss, K. G.; Schäfer, G.; Ackerer, P., Influence of etch pit development on the surface area and dissolution kinetics of the orthoclase (001) surface. *Chem. Geol.* **2016,** *442*, 148-159.

23. Arvidson, R. S.; Collier, M.; Davis, K. J.; Vinson, M. D.; Amonette, J. E.; Lüttge, A., Magnesium inhibition of calcite dissolution kinetics. *Geochim. Cosmochim. Acta* **2006,** *70*, 583-594.

24. Jordan, G.; Rammensee, W., Dissolution rates of calcite (10(1)over-bar4) obtained by scanning force microscopy: Microtopography-based dissolution kinetics on surfaces with anisotropic step velocities. *Geochim. Cosmochim. Acta* **1998,** *62* (6), 941-947.

25. Xu, M.; Hu, X.; Knauss, K. G.; Higgins, S. R., Dissolution kinetics of calcite at 50-70 °C: An atomic force microscopic study under near-equilibrium conditions. *Geochemica and Cosmochimica Acta* **2010,** *74* (15), 285-4297.

26. Duckworth, O. W.; Martin, S. T., Dissolution rates and pit morphologies of rhomoedral carbonate minerals. *Am. Miner.* **2004,** *89* (7), 554-563.

27. Ruiz-Agudo, E.; Putnis, C. V.; Jiménez-López, C.; Rodriguez-Navarro, C., An atomic force microscopy study of calcite dissolution in saline solutions: The role of magnesium ions. *Geochemica and Cosmochimica Acta* **2009,** *73* (11), 3201-3217.

28. Teng, H. H., Controls by saturation state on etch pit formation during calcite dissolution. *Geochim. Cosmochim. Acta* **2004,** *68* (2), 253-262.

29. Bouissonnié, A.; Daval, D.; Marinoni, M.; Ackerer, P., From mixed flow reactor to column experiments and modeling: Upscaling of calcite dissolution rate. *Chem. Geol.* **2018,** *487*, 63-75.

30. Dove, P. M.; Platt, F. M., Compatible real-time reaction rates for in situ imaging of mineral-water interactions using scanning force microscopy. *Chem. Geol.* **1996,** *127*, 331-338.

487 31. Compton, R. G.; Unwin, P. R., The dissolution of calcite in aqueous solution at pH<4:
488 Kinetics and mechanism. *Philosophical Transactions of The Royal Society of London A*
489 *(Mathematical and Physical Sciences)* **1990,** *330* (1609), 1-45.

490 32. Liang, Y.; Baer, D. R.; McCoy, J. M.; Amonette, J. M.; LaFemina, J. P., Dissolution
491 kinetics at the calcite-water interface. *Geochim. Cosmochim. Acta* **1996,** *60* (23), 4883-4887.

492 33. Noiriel, C., Resolving time-dependent evolution of pore scale structure, permeability and
493 reactivity using X-ray microtomography. In *Pore Scale Geochemical Processes. Reviews in*
494 *Mineralogy & Geochemistry Volume 80*, Steefel, C. I.; Emmanuel, E.; Anovitz, L., Eds.
495 Mineralogical Society of America: 2015; pp 247-286.

496 34. Noiriel, C.; Bernard, D.; Gouze, P.; Thibaut, X., Hydraulic properties and
497 microgeometry evolution in the course of limestone dissolution by CO_2-enriched water. *Oil &*
498 *Gas Science and Technology* **2005,** *60* (1), 177-192.

499 35. Godinho, J. R. A.; Withers, P. J., Time-lapse 3D imaging of calcite precipitation in a
500 microporous column. *Geochim. Cosmochim. Acta* **2017,** *222* (Supplement C), 156-170.

501 36. Noiriel, C.; Steefel, C. I.; Yang, L.; Bernard, D., Effects of pore-scale heterogeneous
502 precipitation on permeability and flow *Adv. Water Resour.* **2016,** *95*, 125-137.

503 37. Noiriel, C.; Steefel, C. I.; Yang, L.; Ajo-Franklin, J., Upscaling calcium carbonate
504 precipitation rates from pore to continuum scale. *Chem. Geol.* **2012,** *318-319*, 60–74.

505 38. Blunt, M. J.; Bijeljic, B.; Dong, H.; Gharbi, O.; Iglauer, S.; Mostaghimi, P.; Paluszny,
506 A.; Pentland, C., Pore-scale imaging and modelling. *Adv. Water Resour.* **2013,** *51*, 197-216.

507 39. Cnudde, V.; Boone, M. N., High-resolution X-ray computed tomography in geosciences:
508 A review of the current technology and applications. *Earth-Science Reviews* **2013,** *123*, 1-17.

509 40. Madonna, C.; Quintal, B.; Frehner, M.; Almqvist, B.; Tisato, N.; Pistone, M.;
510 Marone, F.; Saenger, E., Synchrotron-based X-ray tomographic microscopy for rock physics
511 investigations. *Geophysics* **2013,** *78* (1), D53-D64.

41. Marone, F.; Studer, A.; Billich, H.; Sala, L.; Stampanoni, M., Towards on-the-fly data post-processing for real-time tomographic imaging at TOMCAT. *Advanced Structural and Chemical Imaging* **2017,** *3* (1), 1.

42. Villanova, J.; Daudin, R.; Lhuissier, P.; Jauffrès, D.; Lou, S.; Martin, C. L.; Labouré, S.; Tucoulou, R.; Martinez-Criado, G.; Salvo, L., Fast in situ 3D nanoimaging: A new tool for dynamic characterization in materials science. *Materials Today* **2017,** *20* (7), 354-359.

43. Parkhurst, D. L.; Appelo, C. A. J., Description of input and examples for PHREEQC version 3--A computer program for speciation, batch- reaction, one-dimensional transport, and inverse geochemical calculations. In *Techniques and Methods 6-A43, available only at http://pubs.usgs.gov/tm/06/a43*, U.S. Geological Survey 2013; p 497.

44. Stampanoni, M.; Groso, A.; Isenegger, A.; Mikuljan, G.; Chen, Q.; Bertrand, A.; Henein, S.; Betemps, R.; Frommherz, U.; Böhler, P.; Meister, D.; Lange, M.; Abela, R. In *Trends in synchrotron-based tomographic imaging: the SLS experience*, SPIE Optics + Photonics, 2006 San Diego, California, United States, San Diego, California, United States, 2006.

45. Marone, F.; Stampanoni, M., Regridding reconstruction algorithm for real-time tomographic imaging. *Journal of Synchrotron Radiation* **2012,** *19* (6), 1029-1037.

46. Akmal Butt, M.; Maragos, P., Optimum design of chamfer distance transforms. *Image Processing, IEEE Transactions* **1998,** *7* (10), 1477-1484.

47. Russ, J. C., *The Image Processing Handbook, Sixth Edition*. CRC Press: Boca Raton, FL, 2011.

48. MacInnis, I. N.; Brantley, S. L., Development of etch pit size distributions on dissolving minerals. *Chem. Geol.* **1993,** *105* (1), 31-49.

49. de Assis, T. A.; Aarao Reis, F. D. A., Dissolution of minerals with rough surfaces. *Geochim. Cosmochim. Acta* **2018,** *228*, 27-41.

537 50. Plummer, L. N.; Wigley, T. M. L.; Parkhurst, D. L., The kinetics of calcite dissolution in
538 CO_2-water systems at 5° to 60°C and 0.0 to 1.0 atm CO_2. *Am. J. Sci.* **1978,** *278*, 179-216.

539 51. Chou, L.; Garrels, R. M.; Wollast, R., Comparative study of the kinetics and mechanisms
540 of dissolution of carbonate minerals. *Chem. Geol.* **1989,** *78*, 269-282.

541 52. De Giudici, G., Surface control vs. diffusion control during calcite dissolution:
542 Dependence of step-edge velocity upon solution pH. *Am. Miner.* **2002,** *87* (10), 1279-1285.

543 53. Colombani, J., The Alkaline Dissolution Rate of Calcite. *The Journal of Physical*
544 *Chemistry Letters* **2016,** *7* (13), 2376-2380.

545 54. Brunauer, S.; Emmet, P. H.; Teller, E. A., Adsorption of gases in multimolecular layers.
546 *J. Am. Chem. Soc.* **1938,** *60*, 309-319.

547 55. Bibi, I.; Arvidson, R. S.; Fischer, C.; Luttge, A., Temporal evolution of calcite surface
548 dissolution kinetics. *Minerals* **2018,** *8* (6), 256.

549 56. Fischer, C.; Luttge, A., Beyond the conventional understanding of water–rock reactivity.
550 *Earth Planet. Sci. Lett.* **2017,** *457*, 100-105.

551 57. Chen, J. C.; Reischl, B.; Spijker, P.; Holmberg, N.; Laasonen, K.; Foster, A. S., Ab
552 initio Kinetic Monte Carlo simulations of dissolution at the NaCl-water interface. *Physical*
553 *Chemistry Chemical Physics* **2014,** *16* (41), 22545-22554.

554 58. Sjöberg, E. L.; Rickard, D., Temperature dependence of calcite dissolution kinetics
555 between 1 and 62°C at pH 2.7 to 8.4 in aqueous solutions. *Geochim. Cosmochim. Acta* **1984,** *48*,
556 485-493.

557 59. Levenson, Y.; Emmanuel, S., Pore-scale heterogeneous reaction rates on a dissolving
558 limestone surface. *Geochim. Cosmochim. Acta* **2013,** *119*, 188-197.

559 60. Lasaga, A. C.; Luttge, A., Variation of crystal dissolution rate based on a dissolution
560 stepwave model. *Science* **2001,** *291*, 2400-2404.

561 61. Briese, L.; Arvidson, R. S.; Luttge, A., The effect of crystal size variation on the rate of
562 dissolution : A kinetic Monte Carlo study. *Geochim. Cosmochim. Acta* **2017,** *212*, 167-175.

563 62. Kurganskaya, I.; Luttge, A., A comprehensive stochastic model of phyllosilicate
564 dissolution: Structure and kinematics of etch pits formed on muscovite basal face. *Geochim.*
565 *Cosmochim. Acta* **2013,** *120* (0), 545-560.

566

567

568

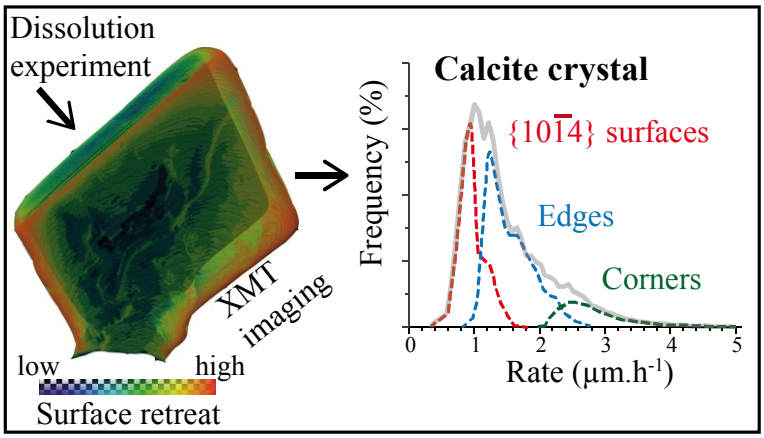

569

570 For TOC only

571